

# Phase modulation beamforming in high frame rate imaging

Brooks D. Lindsey  
Coulter Department of Biomedical Engineering  
Georgia Institute of Technology and Emory University  
Atlanta, GA, USA  
brooks.lindsey@bme.gatech.edu

Bowen Jing  
Coulter Department of Biomedical Engineering  
Georgia Institute of Technology and Emory University  
Atlanta, GA, USA  
bowen.jing@bme.gatech.edu

**Abstract**— While high frame imaging is enabled through the use of unfocused transmit events, images formed from these transmit events have inferior resolution and elevated acoustic clutter relative to images formed with focused transmit beams, even when angular compounding is applied. An approach for forming images with increased resolution is proposed based on introducing very weak aberration into received data, then combining multiple aberrated results and subtracting the aberrated data from the original data without aberration. This approach is demonstrated in simulations, tissue-mimicking phantom experiments, and in vivo imaging. Simulations indicate the full-width half-max (FWHM) of wire targets decreases by  $53.9 \pm 21.1\%$ . In data acquired in a tissue-mimicking phantom at 7.8 MHz, wire target FWHM decreases by  $53.2 \pm 8.7\%$ . In vivo images also reflect the improvements seen in tissue-mimicking phantoms.

**Keywords**—ultrafast, plane wave compounding, aberration, beamforming

## I. INTRODUCTION

Ultrafast plane wave imaging is a useful approach for ultrasound imaging due to its high acquisition rate, with lost spatial and contrast resolution due to the use of unfocused transmit events partially restored by compounding multiple steered transmit events [1]. However, even with plane wave compounding, spatial and contrast resolution are decreased relative to focused transmit events. Recently, several techniques have been presented for improving image quality in plane wave imaging, including optimizing the number of transmit events and maximum steering angle required to maximize image quality for a given array [2], f-k migration methods [3] [4], coherence-based weighting [5] [6], accounting for element directivity [7], applying an angular coherence factor, and suppression of side lobes [8]. In addition, Agarwal et al. have recently presented an approach for high resolution

imaging based on application of multiple anodization functions [9].

One source of degradation in contrast and spatial resolution is aberration, or focusing errors resulting from spatial variations in the speed of sound in tissue. Aberration can be estimated and corrected using acquired radiofrequency (RF) data [10-15]. The point spread function (PSF) can be partially restored by modifying acquired RF data sets prior to beamforming based on time domain estimates of shifts between channel data [10, 14], or alternatively by selecting the phase relationship between adjacent elements that maximizes speckle brightness [13].

In this work, an approach for improving image quality in high frame rate ultrasound imaging with multiple unfocused transmit events is presented based on modifying the phase relationship between received RF channel data prior to beam summation and compounding. This technique introduces small focal errors during receive beamforming, then subtracts the variation resulting from this aberration from non-aberrated data sets to reduce main lobe width. Improved spatial resolution can be demonstrated without increasing the number of transmit events and requiring only parallel delay-and-sum beamforming operations.

## II. METHODS

### A. Processing techniques

Received data are processed two times for each acquisition: 1) using standard delay-and-sum (i.e. without aberration), and 2) with a time delay error introduced across the aperture according to the equation:

$$-A \sin\left(\frac{n\pi}{2}\right) \quad (1),$$

where  $n$  is element number from 1 to 128 and  $A$  is the amplitude of the introduced error, in this case 10 ns (i.e.  $\ll \lambda/10$  at the operating frequency of 7.8 MHz used in this work). For

---

This work was supported in part by the Department of Biomedical Engineering and the College of Engineering at Georgia Institute of Technology and by R01HL144714 from the National Institutes of Health.

conventional delay-and-sum beamforming, receive beamforming delays for a given element  $n$  are computed according to:

$$\tau_{n1}(r_p) = \frac{\|x_{Tx} - x_p\| + \|x_{Rx} - r_p\|}{c} \quad (2),$$

where  $r_p$  is the point in the field  $(x_p, z_p)$ ,  $x_{Tx}$  and  $x_{Rx}$  are the coordinates of the transmit and receiving elements, and  $c$  is the speed of sound. For the case with small focal errors, receive beamforming delays for each element  $n$  are computed according to:

$$\tau_{n2}(r_p) = \tau_{n1}(r_p) - A \sin\left(\frac{n\pi}{2}\right) \quad (3).$$

Delayed signals without focal errors (Equation 2) and with phase errors (Equation 3) are stored in matrices  $\mathbf{X}_{DAS}$  and  $\mathbf{X}_{PM}$ , respectively, for summation. The resulting beamformed RF signal for a given pixel is produced according to:

$$\mathbf{RF}_{DAS}(r_p) = \mathbf{X}_{DAS}^T \mathbf{w} \text{ and } \mathbf{RF}_{PM}(r_p) = \mathbf{X}_{PM}^T \mathbf{w} \quad (4),$$

where  $\mathbf{X}_{DAS}$  and  $\mathbf{X}_{PM}$  contain delayed signals received by an  $n$ -element array from a point at location  $r_p$ , with delays for  $\mathbf{X}_{DAS}$  and  $\mathbf{X}_{PM}$  computed according to equations 2 and 3, respectively, and  $\mathbf{w}$  is an  $n \times 1$  vector with all values equal to one for all depths. This results in two sets of images,  $\mathbf{RF}_{DAS}(x_p, z_p, \alpha)$  and  $\mathbf{RF}_{PM}(x_p, z_p, \alpha)$ , where  $x_p$  and  $z_p$  are lateral and axial coordinates of  $r_p$ , respectively, and  $\alpha$  is the steering angle of the transmitted wave. Images are formed by taking the standard deviation across the multi-angle coherently compounded, envelope-detected versions of  $\mathbf{RF}_{DAS}$  and  $\mathbf{RF}_{PM}$ , then subtracting the normalized result from the conventional image:

$$Image_{Phase Modulation} = \frac{Env\left[\sum_{\alpha=-\alpha_{max}}^{\alpha_{max}} \mathbf{RF}_{DAS}(x_p, z_p, \alpha)\right]}{\max\{Env\left[\sum_{\alpha=-\alpha_{max}}^{\alpha_{max}} \mathbf{RF}_{DAS}(x_p, z_p, \alpha)\right]\}} - \frac{std\left(Env\left[\sum_{\alpha=-\alpha_{max}}^{\alpha_{max}} \mathbf{RF}_{DAS}(x_p, z_p, \alpha)\right], Env\left[\sum_{\alpha=-\alpha_{max}}^{\alpha_{max}} \mathbf{RF}_{PM}(x_p, z_p, \alpha)\right]\right)}{\max\{std\left(Env\left[\sum_{\alpha=-\alpha_{max}}^{\alpha_{max}} \mathbf{RF}_{DAS}(x_p, z_p, \alpha)\right], Env\left[\sum_{\alpha=-\alpha_{max}}^{\alpha_{max}} \mathbf{RF}_{PM}(x_p, z_p, \alpha)\right]\right)} \quad (5),$$

where  $Env[\cdot]$  denotes the envelope of beamformed RF signal,  $\max\{\cdot\}$  denotes the maximum pixel value and  $std(x, y)$  denotes the standard deviation of  $x$  and  $y$ .

In phase modulation beamforming, taking the standard deviation between the envelopes of  $\mathbf{RF}_{DAS}$  and  $\mathbf{RF}_{PM}$  (second term in Equation 5) emphasizes small differences in two similar PSFs; these variations primarily occur along the slope of the main lobe and in the clutter pedestal. When the standard deviation image is subtracted from the conventional delay-and-sum image after compounding and envelope detection (Equation 5), the main lobe width is decreased and the clutter level is also reduced in some locations.

### B. Simulations

Simulations were performed using Field II [16] to mimic the acquisition conditions in the tissue-mimicking phantom (Section C). Briefly, a 128-element linear array transducer operating at

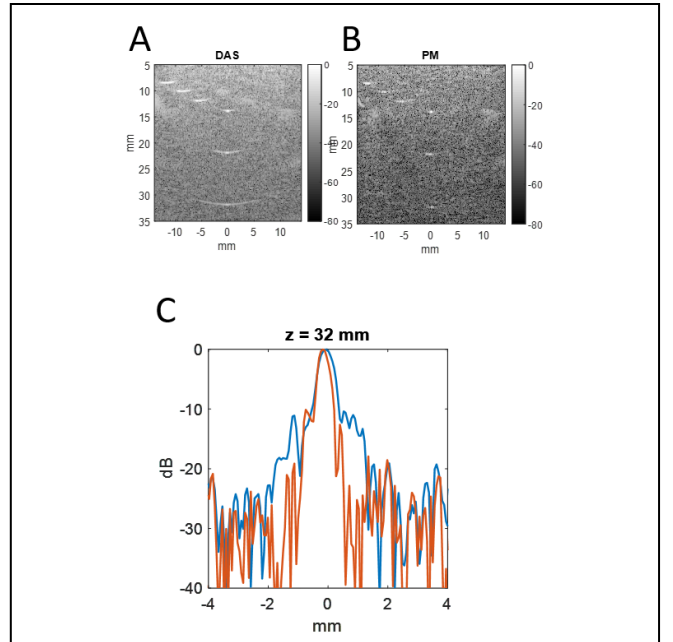


Fig. 1. Simulated images of wire targets in a tissue-mimicking background for (A) delay-and-sum, (B) phase modulation for a single unfocused transmit event. The cross section for the wire target located at  $z=32$  mm is shown in (C).

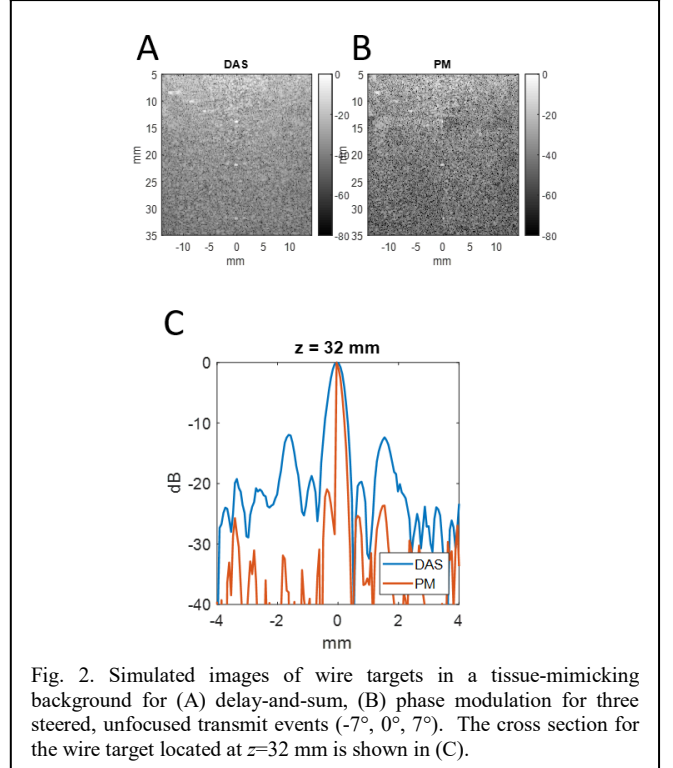


Fig. 2. Simulated images of wire targets in a tissue-mimicking background for (A) delay-and-sum, (B) phase modulation for three steered, unfocused transmit events ( $-7^\circ$ ,  $0^\circ$ ,  $7^\circ$ ). The cross section for the wire target located at  $z=32$  mm is shown in (C).

7.8 MHz was used. Point targets were positioned at depths of 8, 9, 10, 12, 22, and 32 mm as in the physical tissue-mimicking phantom. Weaker scatterers (10 dB lower scattering amplitude relative to point targets) were positioned surrounding these targets ( $>10$  per resolution cell). Radiofrequency (RF) data resulting from these simulations were beamformed offline to produce conventional (delay-and-sum, DAS) and phase modulation images.

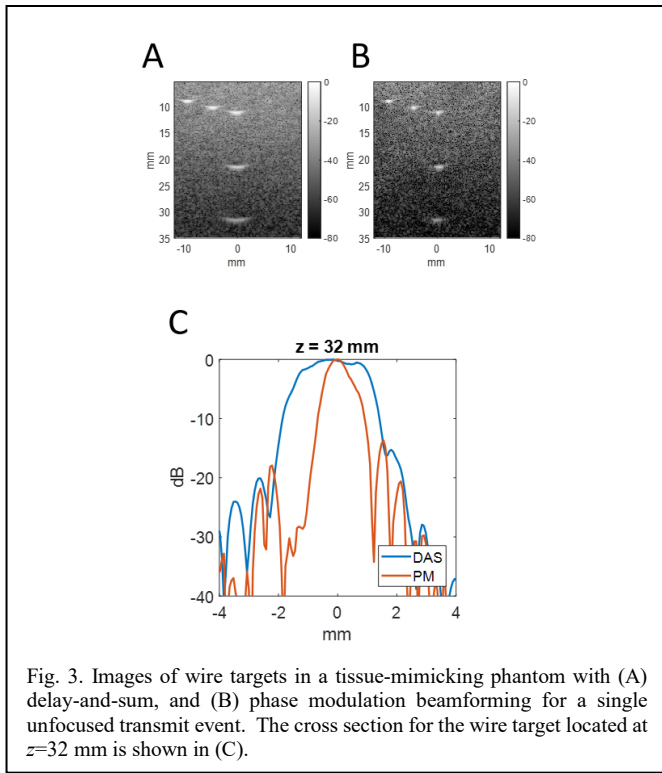


Fig. 3. Images of wire targets in a tissue-mimicking phantom with (A) delay-and-sum, and (B) phase modulation beamforming for a single unfocused transmit event. The cross section for the wire target located at  $z=32$  mm is shown in (C).

### C. Phantom studies

Wire targets were imaged in a tissue-mimicking phantom (ATS Labs Model 539) using a Verasonics Vantage 256 and an L11-5 transducer. Acquired RF data were beamformed offline to produce conventional and phase modulation images.

### D. In vivo imaging

The same L11-5 transducer and system were used to acquire images of the carotid artery and surrounding anatomy in a healthy volunteer.

## III. RESULTS

### A. Simulations

Results of simulations are shown in Fig. 1 for acquisition with a single plane wave transmit event (no compounding) and Fig. 2 for 3 steered transmit events ( $-7^\circ$ ,  $0^\circ$ ,  $7^\circ$ ). The cross-sectional views through the point target at 32 mm shows a decrease in target width in both cases. Across all targets, the decrease in full-width at half maximum (FWHM) was  $53.9 \pm 21.1\%$  for a single transmit event (Table I) and  $47.7 \pm 24.9\%$  for three transmit events (not shown).

### B. Phantom studies

Results of phantom imaging are shown in Fig. 2. In Table II, the change in FWHM in the lateral direction is shown for the wire targets in the tissue-mimicking phantom as a function of depth. The percent change is similar with increasing depth, with only the most shallow wire target showing a smaller improvement.

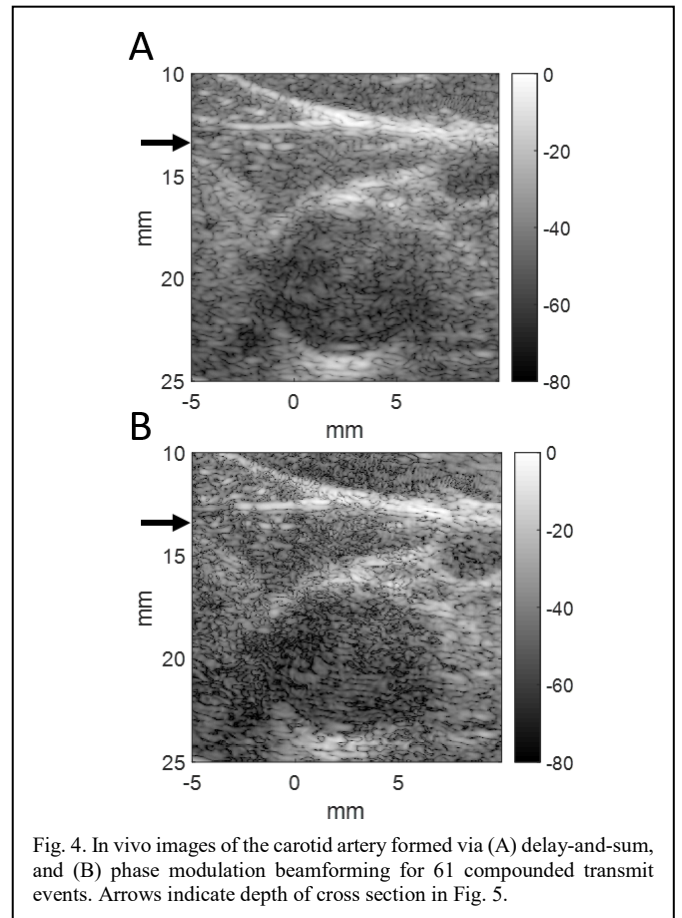


Fig. 4. In vivo images of the carotid artery formed via (A) delay-and-sum, and (B) phase modulation beamforming for 61 compounded transmit events. Arrows indicate depth of cross section in Fig. 5.

TABLE I. SIMULATED POINT TARGET IN TISSUE-MIMICKING PHANTOM

| Depth | FWHM (mm)  |           | Percent change |
|-------|------------|-----------|----------------|
|       | <u>DAS</u> | <u>PM</u> |                |
| 8 mm  | 2.08       | .988      | -52.4%         |
| 9 mm  | 1.82       | 1.13      | -37.7%         |
| 10 mm | 1.18       | 0.310     | -73.9%         |
| 12 mm | 0.482      | 0.092     | -81.0%         |
| 22 mm | 0.695      | 0.521     | -25.0%         |
| 32 mm | 0.99       | 0.461     | -53.8%         |

TABLE II. WIRE TARGETS IN TISSUE-MIMICKING PHANTOM

| Depth | FWHM (mm)  |           | Percent change |
|-------|------------|-----------|----------------|
|       | <u>DAS</u> | <u>PM</u> |                |
| 8 mm  | 0.755      | 0.481     | -36.2%         |
| 9 mm  | 1.15       | 0.536     | -53.4%         |
| 10 mm | 1.38       | 0.614     | -55.5%         |
| 12 mm | 1.55       | 0.604     | -61.0%         |
| 22 mm | 1.94       | 0.827     | -57.3%         |
| 32 mm | 2.87       | 1.27      | -55.7%         |

### C. In vivo imaging

In vivo imaging results are shown in Fig. 4. Point targets such as those in the upper left of the image become visibly narrower, as seen in the cross-section (Fig. 4). Further study is required to evaluate the effect on image contrast and the effect of number of compounding angles on spatial resolution.

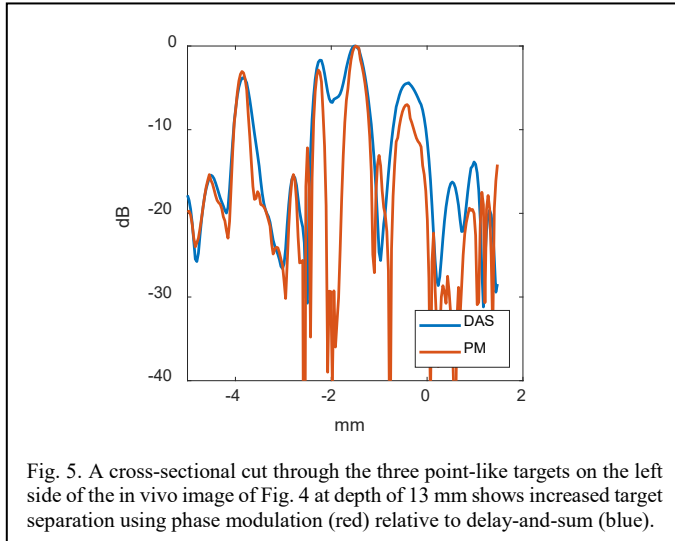


Fig. 5. A cross-sectional cut through the three point-like targets on the left side of the in vivo image of Fig. 4 at depth of 13 mm shows increased target separation using phase modulation (red) relative to delay-and-sum (blue).

### IV. CONCLUSION

Improved spatial resolution can be realized by multiple processing of single received data sets. This processing operates by introducing aberration into received RF data, then subtracting increased sidelobe energy in these aberrated images from the unaberrated image. In phantom studies, the FWHM of wire targets decreased by  $53.2 \pm 8.7\%$ . Increased separation of point-like targets was also visible in vivo (Fig. 4-5).

### REFERENCES

[1] G. Montaldo, M. Tanter, J. Bercoff, N. Benech, and M. Fink, "Coherent Plane-Wave Compounding for Very High Frame Rate Ultrasonography and Transient Elastography," *Ieee Transactions on Ultrasonics Ferroelectrics and Frequency Control*, vol. 56, pp. 489-506, Mar 2009.

[2] J. Jensen, M. B. Stuart, and J. A. Jensen, "Optimized Plane Wave Imaging for Fast and High-Quality Ultrasound Imaging," *IEEE Trans Ultrason Ferroelectr Freq Control*, vol. 63, pp. 1922-1934, Nov 2016.

[3] D. Garcia, L. Le Tarnec, S. Muth, E. Montagnon, J. Poree, and G. Cloutier, "Stolt's f-k Migration for Plane Wave Ultrasound Imaging," *Ieee Transactions on Ultrasonics Ferroelectrics and Frequency Control*, vol. 60, pp. 1853-1867, Sep 2013.

[4] C. Chen, G. Hendriks, R. J. G. van Sloun, H. H. G. Hansen, and C. L. de Korte, "Improved Plane-Wave Ultrasound Beamforming by Incorporating Angular Weighting and Coherent Compounding in Fourier Domain," *IEEE Trans Ultrason Ferroelectr Freq Control*, vol. 65, pp. 749-765, May 2018.

[5] M. Mozumi and H. Hasegawa, "Adaptive Beamformer Combined with Phase Coherence Weighting Applied to Ultrafast Ultrasound," *Applied Sciences-Basel*, vol. 8, Feb 2018.

[6] B. Du, X. Wu, H. Zheng, S. Fang, M. Lu, and R. Mao, "Coherence Plane-Wave Compounding with Angle Coherence Factor for Ultrafast Ultrasound Imaging," *Conf Proc IEEE Eng Med Biol Soc*, vol. 2018, pp. 907-910, Jul 2018.

[7] H. Hasegawa and H. Kanai, "Effect of element directivity on adaptive beamforming applied to high-frame-rate ultrasound," *IEEE Trans Ultrason Ferroelectr Freq Control*, vol. 62, pp. 511-23, Mar 2015.

[8] W. Guo, Y. Y. Wang, and J. H. Yu, "A Sidelobe Suppressing Beamformer for Coherent Plane Wave Compounding," *Applied Sciences-Basel*, vol. 6, Nov 2016.

[9] A. Agarwal, J. Reeg, A. S. Podkowa, and M. L. Oelze, "Improving Spatial Resolution Using Incoherent Subtraction of Receive Beams Having Different Apodizations," *Ieee Transactions on Ultrasonics Ferroelectrics and Frequency Control*, vol. 66, pp. 5-17, Jan 2019.

[10] S. Krishnan, K. W. Rigby, and M. O'Donnell, "Adaptive aberration correction of abdominal images using PARCA," *Ultrason Imaging*, vol. 19, pp. 169-79, Jul 1997.

[11] N. M. Ivancevich, J. J. Dahl, and S. W. Smith, "Comparison of 3-D multi-lag cross-correlation and speckle brightness aberration correction algorithms on static and moving targets," *IEEE Trans Ultrason Ferroelectr Freq Control*, vol. 56, pp. 2157-66, Oct 2009.

[12] B. D. Lindsey and S. W. Smith, "Pitch-catch phase aberration correction of multiple isoplanatic patches for 3-D transcranial ultrasound imaging," *IEEE Trans Ultrason Ferroelectr Freq Control*, vol. 60, pp. 463-80, Mar 2013.

[13] L. Nock, G. E. Trahey, and S. W. Smith, "Phase Aberration Correction in Medical Ultrasound Using Speckle Brightness as a Quality Factor," *Journal of the Acoustical Society of America*, vol. 85, pp. 1819-1833, May 1989.

[14] S. W. Flax and M. Odonnell, "Phase-Aberration Correction Using Signals from Point Reflectors and Diffuse Scatterers - Basic Principles," *Ieee Transactions on Ultrasonics Ferroelectrics and Frequency Control*, vol. 35, pp. 758-767, Nov 1988.

[15] G. Chau, M. Jakovljevic, R. Lavarello, and J. Dahl, "A Locally Adaptive Phase Aberration Correction (LAPAC) Method for Synthetic Aperture Sequences," *Ultrason Imaging*, vol. 41, pp. 3-16, Jan 2019.

[16] J. A. Jensen and N. B. Svendsen, "Calculation of Pressure Fields from Arbitrarily Shaped, Apodized, and Excited Ultrasound Transducers," *Ieee Transactions on Ultrasonics Ferroelectrics and Frequency Control*, vol. 39, pp. 262-267, Mar 1992.